The Planetary Science Journal, 4:230 (9pp), 2023 December https://doi.org/10.3847/PSJ/ad08c1

Synthetic Detections of Interstellar Objects with the Rubin Observatory Legacy Survey of Space and Time

Dušan Marčeta[1] and Darryl Z. Seligman[2,3]
[1] Department of Astronomy, Faculty of Mathematics, University of Belgrade, Studentski trg 16, Belgrade, 11000, Serbia; dusan.marceta@matf.bg.ac.rs
[2] Department of Astronomy and Carl Sagan Institute, Cornell University, 122 Sciences Drive, Ithaca, NY 14853, USA
Received 2023 June 29; revised 2023 October 21; accepted 2023 October 26; published 2023 December 6

Abstract

The discovery of two interstellar objects passing through the solar system, 1I/'Oumuamua and 2I/Borisov, implies that a galactic population exists with a spatial number density of order $\sim$0.1 au^{-3}. The forthcoming Rubin Observatory Legacy Survey of Space and Time (LSST) has been predicted to detect more asteroidal interstellar objects like 1I/'Oumuamua. We apply recently developed methods to simulate a suite of galactic populations of interstellar objects with a range of assumed kinematics, albedos, and size–frequency distributions (SFDs). We incorporate these populations into the objectsInField algorithm, which simulates detections of moving objects by an arbitrary survey. We find that the LSST should detect between $\sim$0 and 70 asteroidal interstellar objects every year (assuming the implied number density), with sensitive dependence on the SFD slope and characteristic albedo of the host population. The apparent rate of motion on the sky—along with the associated trailing loss—appears to be the largest barrier to detecting interstellar objects. Specifically, a relatively large number of synthetic objects would be detectable by the LSST if not for their rapid sky motion ($>0.^\circ5$ day^{-1}). Therefore, algorithms that could successfully link and detect rapidly moving objects would significantly increase the number of interstellar object discoveries with the LSST (and in general). The mean diameter of detectable, inactive interstellar objects ranges from $\sim$50 to 600 m and depends sensitively on the SFD slope and albedo.

Unified Astronomy Thesaurus concepts: Interstellar objects (52)

1. Introduction

The source reservoirs of small bodies within the solar system have long been the subject of investigation. The isotropically distributed in inclination long-period comets stem from the spherical Oort Cloud (Oort 1950), which has a total mass of $\sim$1–20 $M_\oplus$ (Francis 2005; Kaib & Quinn 2009; Brasser & Morbidelli 2013; Dones et al. 2015). Meanwhile, the low-inclination short-period comets come from the Kuiper Belt objects (Jewitt & Luu 1993). The Kuiper Belt and Oort Cloud were presumably populated during significant and early orbital migration of the giant planets (Hahn & Malhotra 1999; Gomes et al. 2004; Morbidelli et al. 2005; Tsiganis et al. 2005; Nesvorný 2018). However, only a small fraction, $\sim$1%–10%, of scattered objects populated the Kuiper Belt and Oort Cloud (Hahn & Malhotra 1999; Brasser et al. 2010; Dones et al. 2015; Higuchi & Kokubo 2015). The solar system likely generated $\sim$1–30 $M_\oplus$ of material in interstellar comets (Seligman & Moro-Martín 2023).

The discovery of the first interstellar object (ISO) 1I/'Oumuamua implies that a galactic source population exists with a spatial number density of order $\sim n_o \sim 1 \times 10^{-1}$ au^{-3} (Laughlin & Batygin 2017; Trilling et al. 2017; Do et al. 2018; Levine et al. 2021). Extrapolation of this spatial number density to an isotropic galactic population of similar objects implies that on average $\sim$1 $M_\oplus$ of material is ejected by every stellar system (Jewitt & Seligman 2023). Therefore, the discovery of future interstellar interlopers appears to be imminent.

For recent reviews of this field, we refer the reader to Jewitt & Seligman (2023), Moro-Martín (2022), Fitzsimmons et al. (2023), and Seligman & Moro-Martín (2023). 1I/'Oumuamua was discovered on 2017 October 19 (Williams et al. 2017) with the Pan-STARRS telescope (Chambers et al. 2016). It lacked a cometary tail (Jewitt et al. 2017; Meech et al. 2017; Ye et al. 2017) and had a slightly reddened reflectance spectra (Bannister et al. 2017; Masiero 2017; Bolin et al. 2018; Fitzsimmons et al. 2018), an elongated shape (Bannister et al. 2017; Jewitt et al. 2017; Knight et al. 2017; Meech et al. 2017; Belton et al. 2018; Bolin et al. 2018; Drahus et al. 2018; Fraser et al. 2018; Mashchenko 2019), a low incoming velocity with respect to the local standard of rest (Gaidos et al. 2017; Mamajek 2017; Hallatt & Wiegert 2020; Hsieh et al. 2021), and a nongravitational acceleration (Micheli et al. 2018). It has been hypothesized that 1I/'Oumuamua is a porous fractal aggregate (Sekanina 2019a; Flekkøy et al. 2019; Moro-Martín 2019; Luu et al. 2020) or a sublimating icy comet with little dust production (Füglistaler & Pfenniger 2018; Sekanina 2019b; Seligman & Laughlin 2020; Desch & Jackson 2021; Jackson & Desch 2021; Levine & Laughlin 2021; Levine et al. 2021; Desch & Jackson 2022; Bergner & Seligman 2023).

A second ISO, 2I/Borisov, was discovered 2 yr later in 2019. The object had a nuclear radius estimated to be 0.2–0.5 km (Jewitt & Luu 2019; Jewitt et al. 2020a) and a distinct coma (de León et al. 2019; Jewitt & Luu 2019; Bolin et al. 2020b; Guzik et al. 2020; Hui et al. 2020; Mazzotta Epifani et al. 2021). The object had some nontypical properties, including a hypervolatile enriched composition (Bodewits et al. 2020; Cordiner et al. 2020), high polarization of dust in the outflow (Bagnulo et al. 2021; Halder & Sengupta 2023), and a

[3] NSF Astronomy and Astrophysics Postdoctoral Fellow.

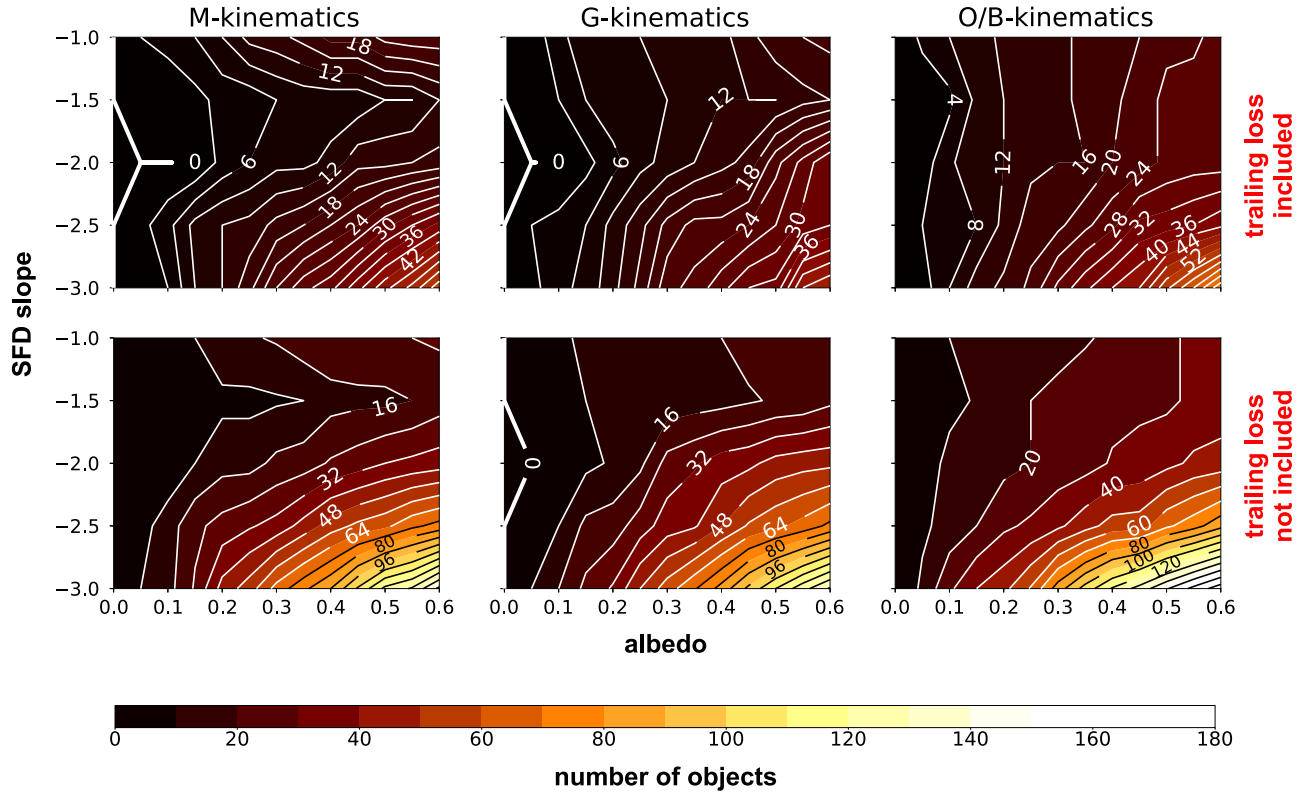

Figure 1. The total number of detectable ISOs per year. The top and bottom panels show this number when the effects of trailing loss are included and excluded, respectively. The detectability criterion requires at least three detections in the synthetic LSST frames. The trailing loss depends on the exposure time and FWHM. Here we adopt a $0''.7$ for FWHM and 30 s exposure time, as given in Jones et al. (2018). We cut the albedo axis at 0.6 because the number of asteroids expected beyond this value is considered negligible (Mainzer et al. 2012).

disintegration event (Bolin et al. 2020a; Jewitt et al. 2020b, 2020c; Drahus et al. 2020; Kim et al. 2020; Zhang et al. 2020).

There have been significant efforts to characterize the prospects for detecting ISOs in the solar system. The forthcoming Rubin Observatory Legacy Survey of Space and Time (LSST; Jones et al. 2009; Ivezić 2019) should efficiently detect transient objects (Solontoi & Ivezić 2011; Vereš & Chesley 2017, 2017; Jones et al. 2018). Moreover, the forthcoming NEO Surveyor (Mainzer et al. 2015) should also detect ISOs. There has been significant effort invested in estimating the rate at which the LSST will discover ISOs, which has been most recently estimated at one to three objects per year (Hoover et al. 2022). Flekkøy & Toussaint (2023) concluded that the LSST should detect a second 'Oumuamua-like ISO in <5 yr after the survey starts with 90% confidence. Previously, Rice & Laughlin (2019) concluded that LSST should be able to detect over 100 objects per year with radii larger than 1 m. These estimates naturally contrast with those provided prior to the discovery of 1I/'Oumuamua and 2I/Borisov (Moro-Martín et al. 2009), which projected a low probability for LSST to detect an ISO during its operational lifetime.

The most straightforward method to calculate the distribution of expected trajectories is via a Monte Carlo integration, defined as the "dynamical method" (Marčeta 2023) and implemented in Cook et al. (2016), Engelhardt et al. (2017), Seligman & Laughlin (2018), and Hoover et al. (2022). Alternatively, the analytic "probabilistic method" is orders of magnitude more computationally efficient (Marčeta 2023). In this paper, we implement the probabilistic method in conjunction with the objectsInField (OIF; Cornwall et al. 2020) software to estimate the population of ISOs that will be discovered with the LSST. Given the computational efficiency of the method, we are able to produce synthetic survey results for a range of assumed size–frequency distributions (SFDs), albedos, and kinematics.

This paper is organized as follows: In Section 2, we describe the methodology of our study, primarily focusing on an overview of the previously reported probabilistic method (Marčeta 2023) and our implementation of the LSST observability criteria. In Section 3 we present the results of the distribution of ISOs that will be detectable by LSST as a function of the assumed SFD slope, albedo, and background stellar kinematics of the galactic population. In Section 4 we conclude.

2. Methods

2.1. Overview of Probabilistic Method

The method that we use to generate the population is briefly described in this section. The probabilistic method calculates the distributions of orbital elements of ISOs as a function of the assumed kinematic distribution. It is orders of magnitude more computationally efficient than the dynamic method that has previously been implemented by Cook et al. (2016), Engelhardt et al. (2017), Seligman & Laughlin (2018), and Hoover et al. (2022). Specifically, starting from the assumption of conservation of the total number of ISOs in an arbitrary sphere around the Sun, it derives the joint probability density functions of six

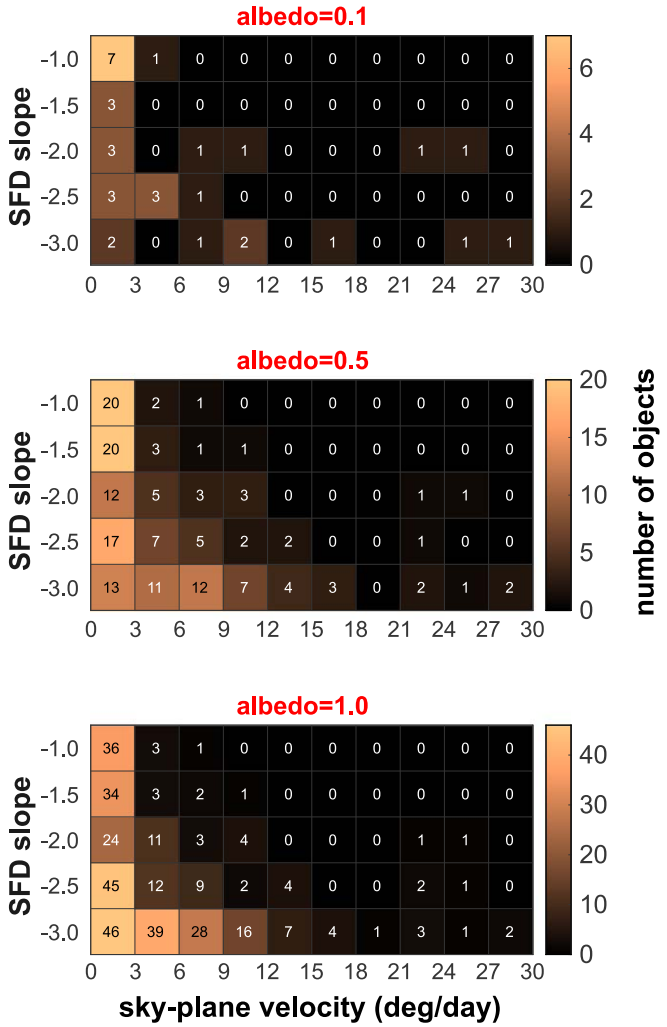

Figure 2. The apparent rate of sky motion of ISOs as a function of the SFD slope. The three panels correspond to three assumed albedos for each object in the synthetic populations. The rates of motion are orders of magnitude higher than for typical solar system objects.

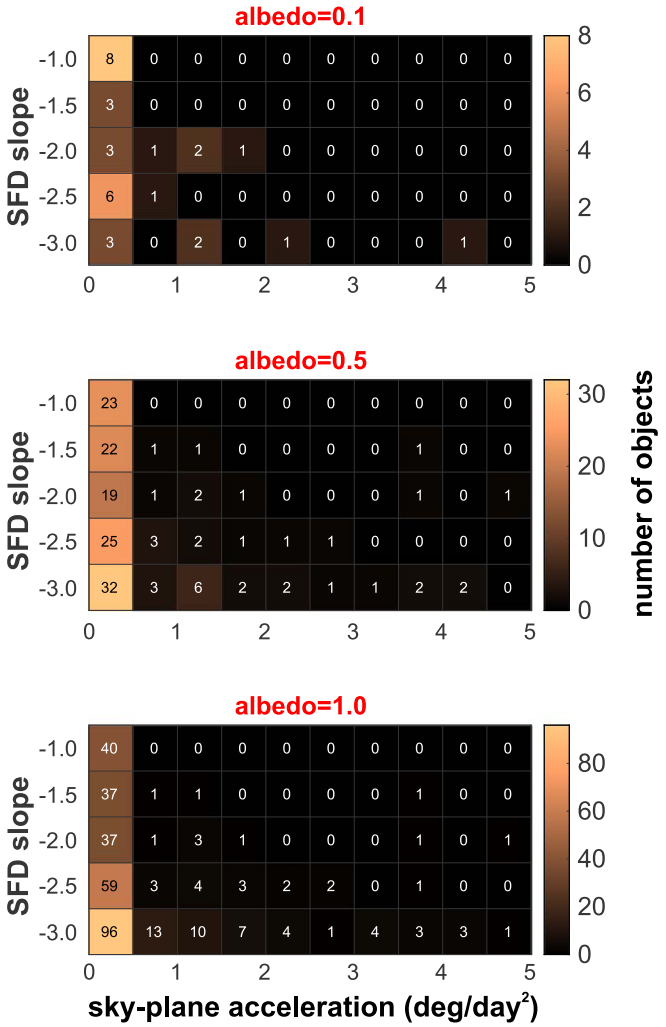

Figure 3. Same as Figure 2, but for the acceleration of the sky motion. We only show the absolute value of the apparent acceleration because the sign does not impact the detectability.

parameters that define orbits of ISOs in the form

$$p = \begin{cases} \frac{v_\infty p}{4\pi r} \frac{B}{\sqrt{v_\infty^2 r^2 + 2\mu r - B^2 v_\infty^2}}, & B \leqslant B_1 \\ \frac{v_\infty p}{2\pi r} \frac{B}{\sqrt{v_\infty^2 r^2 + 2\mu r - B^2 v_\infty^2}}, & B_1 < B \leqslant B_2 \end{cases}, \quad (1)$$

where μ is the gravitational parameter of the Sun, v_∞ is excess velocity, r is heliocentric distance, B is impact parameter, B_1 and B_2 are critical impact parameters defining whether an object hits the Sun ($B < B_1$) or misses the heliocentric sphere with radius r ($B > B_2$), and p represents the kinematics of the population in interstellar space (i.e., distribution of interstellar velocity components with respect to the local standard of rest).

The probabilistic method incorporates the gravitational focusing from the Sun by construction (see Section 2 in Marčeta 2023). This method can incorporate any assumed kinematic distribution of ISOs. In this paper, we simulate ISOs assuming that they exhibit the same kinematics as M-, G-, and O/B-star populations (see the discussion in Seligman & Laughlin 2018; Hoover et al. 2022; Marčeta 2023).

2.2. LSST Observability Criteria: objectsInField Implementation

Cornwall et al. (2020) presented open-source software OIF. This software simulates a realistic LSST campaign that incorporates observation scheduling. Specifically, we utilized the cadence labeled *kraken_2026*, which is widely considered as a top candidate for the observational baseline cadence. This and other cadences are described in detail in the Alternate Observing Strategies.[4] Certain alternative strategies involve only minor modifications to *kraken_2026* (e.g., *colossus_2665*) and are not expected to significantly impact the performance for ISO detections. However, some other proposed cadences employ significantly different strategies, such as the rolling cadence (e.g., *kraken_2036*). These alternative strategies focus on a single region of the sky at a time instead of spreading observations across the entire visible sky every few days. Performance estimation of these strategies would therefore require a separate systematic analysis for ISOs and solar system objects (Schwamb et al. 2023).

The OIF software uses a synthetic solar system model developed by Grav et al. (2011). This package generates a list

[4] https://docushare.lsst.org/docushare/dsweb/Get/Document-28716

of candidate detections for an input population of moving objects in a specified list of field pointings. This tool only provides objects that will appear in each specific field of view (FOV). There will be about 2.4 million FOVs over 10 yr of the survey. However, the software does not assess the detectability of the object and identify which trajectories would realistically be detected. Therefore, our nominal detections are simply objects that will appear bright enough in a realistic LSST FOV. We transformed diameters to absolute magnitudes according to the conversion formula (see, e.g., Bowell et al. 1989; Pravec & Harris 2007)

$$H = 15.618 - 2.5\log_{10}(\text{albedo}) - 5\log_{10}(D), \quad (2)$$

where the diameter, D, has units of kilometers. An apparent visual magnitude is then calculated by OIF as

$$V = H + 5\log_{10}(\Delta) + 5\log_{10}(r_h) - \Phi. \quad (3)$$

In Equation (3), the phase function, Φ, is calculated according to

$$\begin{aligned}\Phi &= 2.5\log_{10}((1-G)\cdot\varphi_1 + G\cdot\varphi_2),\\ \varphi_1 &= \exp\left(-A_1\tan^{B_1}\left(\frac{\phi}{2}\right)\right),\\ \varphi_2 &= \exp\left(-A_2\tan^{B_2}\left(\frac{\phi}{2}\right)\right),\end{aligned} \quad (4)$$

where $A_1 = 3.33$, $A_2 = 1.87$, $B_1 = 0.63$, $B_2 = 1.22$, $G = 0.15$, and ϕ is a phase angle.

We consider an object detected if it reaches a visual magnitude of 24.38, which corresponds to the expected average 5σ limiting magnitude in the g filter. Furthermore, we require that objects have at least three detections to be included in the detected population. A linking algorithm could optimistically connect three trailed detections into a preliminary orbit. The rate of transforming these detections into discoveries relies on the linking algorithms' capacity to connect detections with a range of relevant features. For example, the algorithm would need to overcome ISO sky-plane velocities and accelerations that are much more rapid than those of any solar system populations.

3. Results

In this section, we describe the results of our synthetic population synthesis. We initiate the population at a heliocentric distance of 30 au. This is the maximum initial heliocentric distance from which the brightest object ($D = 1$ km, albedo $= 1$) can reach a distance where it can be observed ($\sim$8 au) in a 1 yr simulation time. We assume that the population begins with every object having an albedo of 1.0, and we then scale the analysis for a variety of albedos.

3.1. Number of Interstellar Objects Detectable with LSST

We generate synthetic populations for a range of assumed SFDs. We simulated objects assuming that the sizes range from 10 to 1000 m, although the results are not sensitive to the exact cutoff size. Objects larger than 1 km are very rare in general. On the other hand, objects smaller than 10 m are very faint and rapidly moving. All of these objects are normalized to the spatial number density of 0.1 au^{-3} for objects larger than 100 m in diameter, implied by the detection of 1I/'Oumuamua for similarly sized bodies.

We restrict our analysis to asteroidal ISOs. A similar analysis will be conducted incorporating a variety of cometary brightening models to estimate the total number of detectable active interstellar comets. This analysis will also assess the extent to which selection effects impact the ratio of cometary to asteroidal detections and how this reflects the properties of the underlying true populations.

In Figure 1, we show the number of ISO detections per year with the LSST as a function of assumed albedo and SFD. The criterion for detection is that the object is detected at least 3 times. These detections may occur on the same or on different nights. This could prove to be a crucial issue based on the linking algorithms used on the LSST data (Holman et al. 2018; Jones et al. 2018). This analysis can be reperformed using different detection criteria to modify the synthetic survey results.

We use the OIF algorithm to simulate the synthetic detections. We perform the simulations for a range of assumed albedo and SFDs (described by a power law $N(D) \propto D^q$), where the albedo ranges from 0 to 1 and the SFD slope q ranges from -3 to -1. This is intended to cover a substantial portion of possible realistic populations. We also show the same plot assuming (i) M, (ii) G, and (iii) O/B kinematics for the kinematic distributions of ISOs. It is apparent that the number of detectable objects with LSST varies between $\sim$0 and 70 yr^{-1} based on the underlying kinematics, SFD slope, and albedo of the population, as shown in the top panels of Figure 1, which include the effect of trailing loss.

We account for trailing loss in our synthetic detections, which is especially important for rapidly moving, inactive ISOs. Trailing loss occurs when an object's motion causes its photons to spread across a broader area than a typical stellar point-spread function. This effect is quantified by employing the function (Jones et al. 2018)

$$\begin{aligned}\Delta m &= -1.25\log_{10}\left(1 + \frac{ax^2}{1+bx}\right),\\ x &= \frac{vT_{\text{exp}}}{24\theta},\end{aligned} \quad (5)$$

where v is the sky-plane velocity (in deg/day), T_{exp} is the exposure time (in seconds), and θ is the FWHM (in arcseconds). Jones et al. (2018) found that the parameter values $a = 0.67$ and $b = 1.16$ best describe trailing signal-to-noise ratio losses. We employ $\theta = 0.7$, which is expected to represent the median seeing,[5] and $T_{\text{exp}} = 30$, s, corresponding to the *kraken_2026* cadence.

In the bottom panels of Figure 1 we show the number of detected objects without including the trailing loss in the calculation. It is evident that the number of detectable objects increases by a factor of $\sim$3–4 when the trailing loss is not incorporated. The reason for this is that the ISOs tend to travel extremely fast and have high apparent rates of sky motion. This proportion grows as the SFD slope increases and the characteristic albedo decreases. However, the only scenarios resulting in 0 detections are those with (i) an albedo below 0.1, (ii) an SFD slope of -2, and (iii) M and G kinematics when the trailing loss is included. This analysis strongly supports the conclusion that, based on the assumed number density, LSST will consistently detect ISOs. In addition, it is possible that the

[5] Seeing values for LSST strategy simulations: https://rtn-022.lsst.io

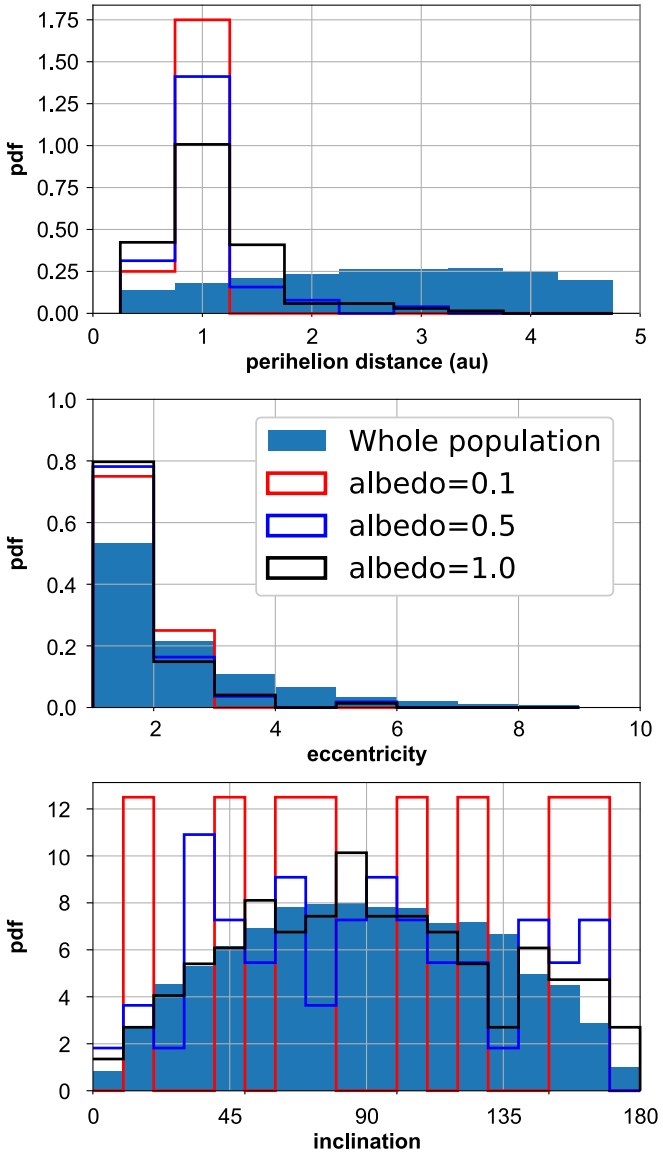

Figure 4. The perihelion distance (top), eccentricity (middle), and inclination (bottom) of detectable ISOs. The underlying population has an SFD slope of −3, and each object has an albedo of 0.1. We show the distributions for the entire population without the detectability constraints (blue filled) and for cases where the albedo is 0.1 (red open), 0.5 (blue open), and 1.0 (black open).

number densities inferred for this population from the detections of 1I/'Oumuamua and 2I/Borisov are underrepresenting the true number density, simply because the population of objects move too rapidly and are undetectable owing to trailing loss. Moreover, if techniques are developed to detect objects that are very rapidly moving, then our estimates for the detection would increase.

For the remainder of this work, all other results are shown using only O/B kinematics. This choice is motivated because, for a given number density, these younger stellar populations yield the largest number of objects, yielding the most computationally efficient statistics. This is due to the fact that these young stars have smaller velocity dispersions, and therefore the solar gravitational focusing is more efficient and produces a larger number of objects close to the Sun. Given that there are already a large number of parameters, we elected not to show the remaining results for all three kinematics.

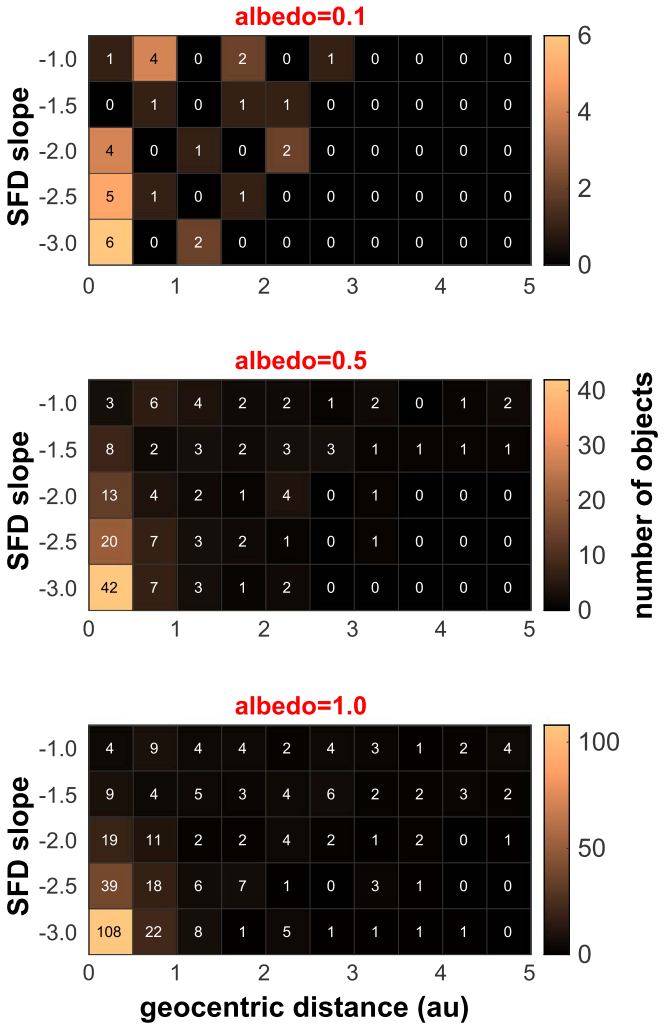

Figure 5. The distribution of geocentric distance of detectable ISOs when they attain maximum brightness.

However, the kinematic distribution of ISOs is entirely unconstrained, as is the relative contribution of different star populations. Furthermore, Hopkins et al. (2023) suggest that the ISO population should be drawn not only from the current stellar populations but also from a so-called sin morte population of stars, encompassing all stars since the birth of the galaxy. Once the kinematic distribution of ISOs is better constrained via future detections, these results can be updated.

3.2. Sky Motion Statistics

In Figures 2 and 3 we show the apparent rate of motion and acceleration of detectable objects as a function of the SFD slope and albedo. It is evident that there are many objects that cannot be tracked by traditional algorithms because they are moving much faster than the proposed limits for apparent motion of $0.^{\circ}5\ \mathrm{day}^{-1}$ (Jones et al. 2018). This also applies to the apparent acceleration.

An increase in the SFD slope generally leads to an increase in the number of rapidly moving objects. This is because the smaller objects must exhibit closer approaches to Earth in order to be detectable, and they are therefore moving much more rapidly. A nontrivial corollary to this is that the distribution of sky motions of ISOs provides information regarding the SFD.

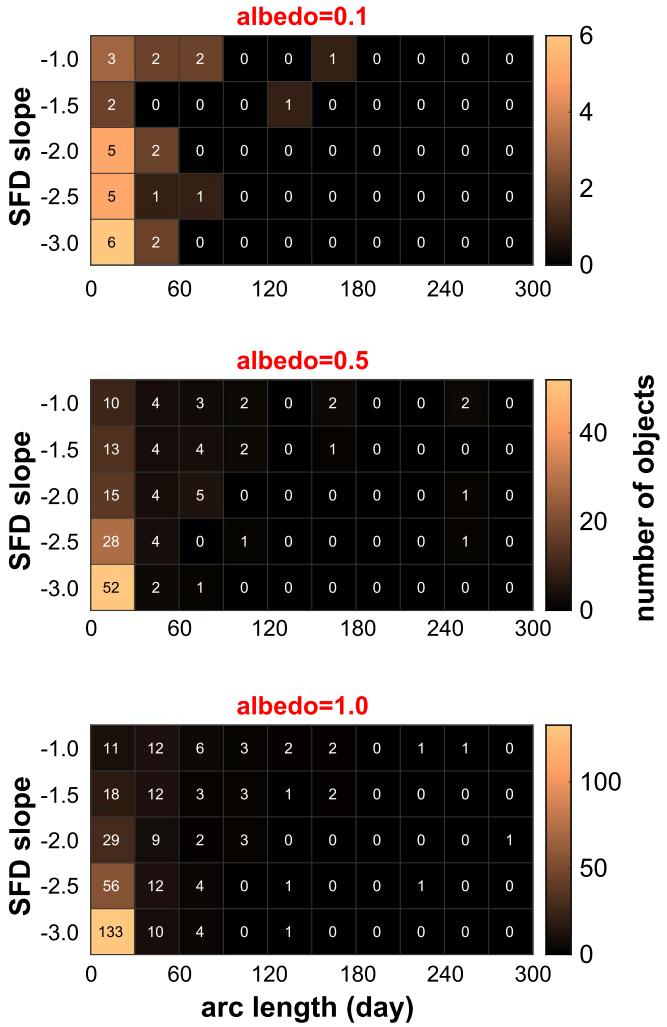

Figure 6. The distribution of arc length during which a synthetic ISO is detectable.

3.3. Trajectories of Interstellar Objects

In Figure 4 we show the perihelion distance, eccentricity, and inclination for the detected populations. By renormalizing, we also show the corresponding distributions for the entire population. The different color histograms correspond to detectable objects with albedos of 0.1, 0.5, and 1. The eccentricity distribution is independent of albedo, but the peak for perihelion distance at 1 au increases when the albedo decreases. The inclination distribution converges to the underlying distribution of inclination for the higher-albedo cases. However, there are only eight objects in the low-albedo case, which is an insufficient sample size for statistical measurement.

In Figure 5 we show the distribution of the geocentric distance of objects when they are at maximal brightness. These distributions are straightforward to interpret. In the case of a low assumed albedo for the population, the detections are mostly at small geocentric distances. When a larger albedo is assumed, there are some detections at larger distances. These more distant objects most likely have smaller rates of motion as well.

In Figure 6 we show the arc length for which an object is detectable for each detectable object in the populations. A smaller albedo assumed for the population produces shorter arcs in general. The short arcs also dominate the high-albedo

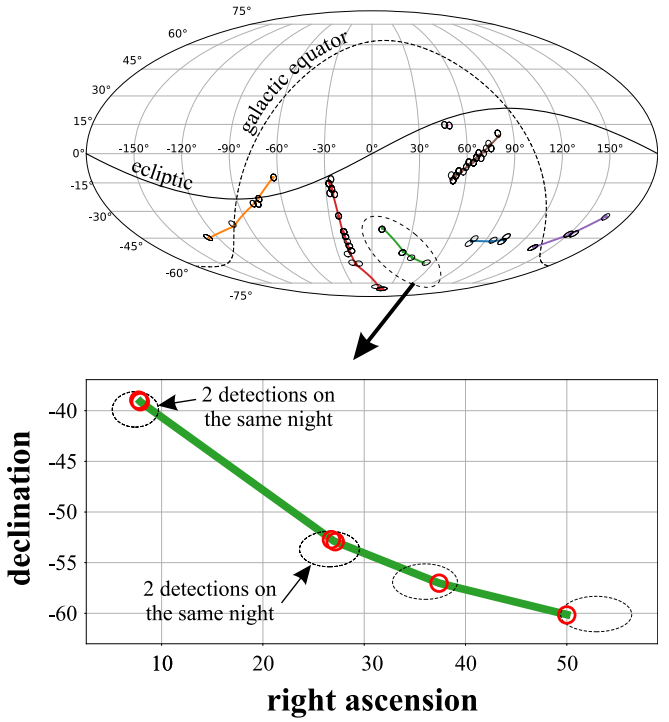

Figure 7. Examples of sky paths of synthetic detectable objects (top panel). The individual points show individual detections with the OIF simulation. We show one zoomed-in region (indicated in the top panel in the dashed circular region) including a synthetic ISO path with six detections (bottom panel). These plots are obtained assuming an SFD of −2.5 (an intermediate value), albedo of 0.1 (conservative), and O/B kinematics.

cases owing to the large number of small objects in each population. In general, objects are detectable for <1–2 months.

In Figure 7 we show examples of sky paths of detected synthetic objects on the sky plane. The individual points show individual detections with the OIF simulation. These plots are obtained for SFD −2.5, albedo = 0.1, and O/B kinematics. We also required that the object be within the LSST FOV for every synthetic detection. Synthetic ISOs are typically moving rapidly and often do not appear in the same FOV twice during one night. As evident from the figure, the typical paths and detection patterns are diverse.

In Figures 8 and 9 we show the duration of time that ISOs spend within 5 au. We show this for the detectable population (Figure 8) and the entire population (Figure 9). This parameter is a critical component in calculating detection rates because it is used in conjunction with the number density to estimate rates. The time spent within the 5 au sphere is relatively insensitive to the albedo and SFD. Moreover, the median is ∼1–2 yr for all populations. The distribution in Figure 9 is skewed toward shorter times. This is because there are relatively more objects with large perihelion distances. These objects only barely pass within the 5 au sphere. However, these distant objects are never detectable. Detectable objects, on the other hand, have smaller perihelion distances with more curved orbits and spend significantly more time inside the sphere.

3.4. Sizes

In Figure 10 we show the distribution of sizes of detectable objects for a range of SFD and albedo. Populations with low values of the SFD slopes produce a relatively uniform distribution of sizes of detectable objects. On the other hand,

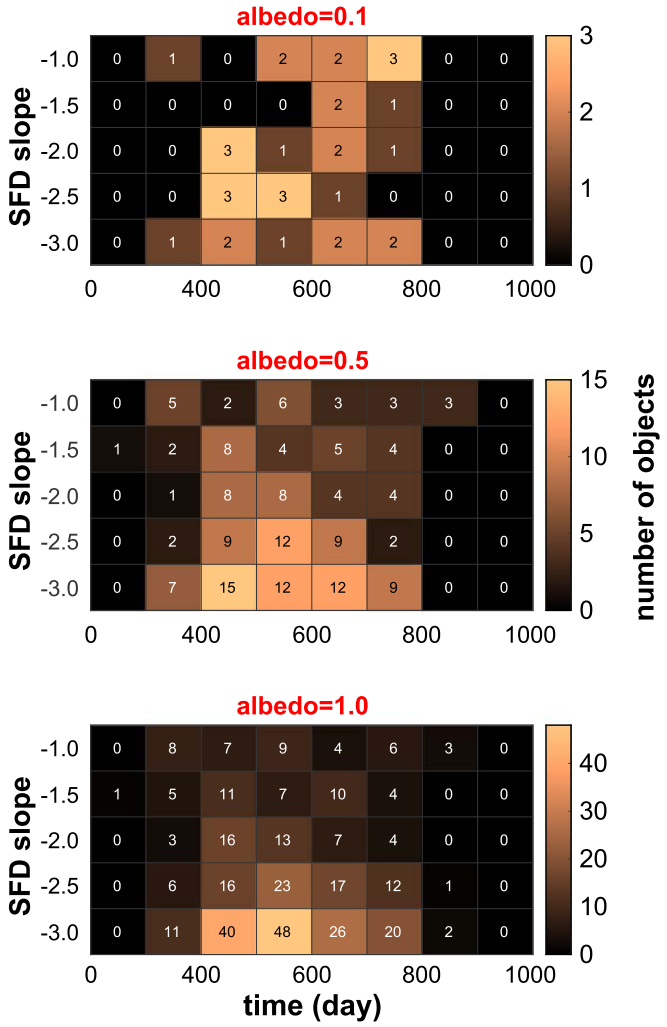

Figure 8. The amount of time a detectable ISO spends inside of the 5 au sphere for a range of albedo and SFD slope.

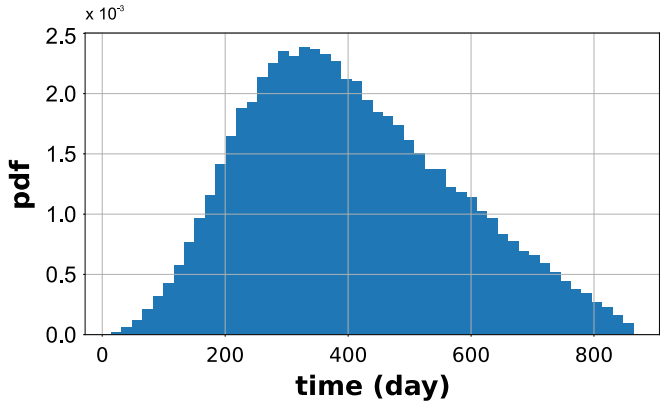

Figure 9. The amount of time an ISO spends inside of the 5 au sphere for O/B kinematics. This distribution is for the entire population and is not filtered by detectable objects.

populations with larger SFD slopes produce many more small detectable objects. This is also the case for the entire population. In general, ISOs in the 100 m size range are more likely to be detected for a steeper SFD. We conclude that given that 1I/'Oumuamua was the first object discovered, this is tentative evidence for a steeper SFD of ISOs. We note that this

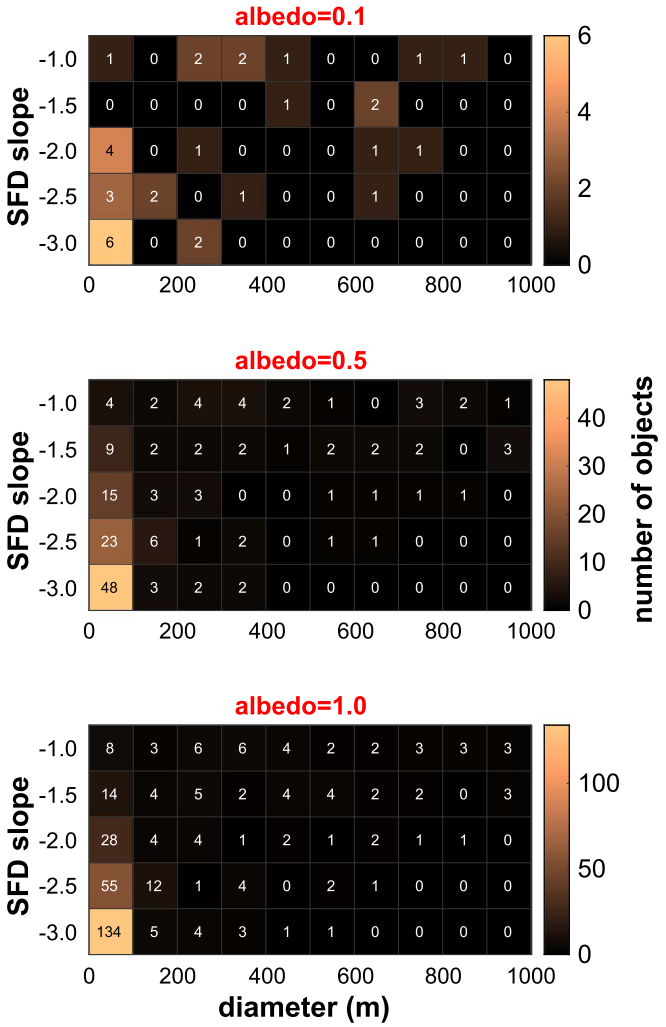

Figure 10. The distribution of the diameters of synthetic ISOs detectable with the LSST.

conjecture is highly speculative, and the inherent SFD will be constrained with future detections.

In Figure 11 we show the median and mean diameters of detectable objects as a function of albedo and SFD slope. The typical sizes of ISOs detected in the future with the LSST will be between 50 and 600 m based on the SFD and albedo. It appears that the diameter of detectable ISOs is relatively sensitive to the SFD and insensitive to the albedo. Moreover, it is possible that the detectability of smaller objects is more heavily affected by the trailing loss (Figure 1) than that of larger objects. This may contribute to the lack of detections of smaller ISOs, although future work is required to quantify this effect.

4. Discussion

In this paper, we generated a synthetic population of ISOs following the methodology developed in Marčeta (2023), assuming different kinematics and a range of SFDs. We then implemented the OIF algorithm to generate realistic LSST survey conditions and evaluated the ISOs that would be detectable with the LSST. We required for detectability that the objects appeared bright enough in the LSST frames and produced at least three detections, regardless of the nights on

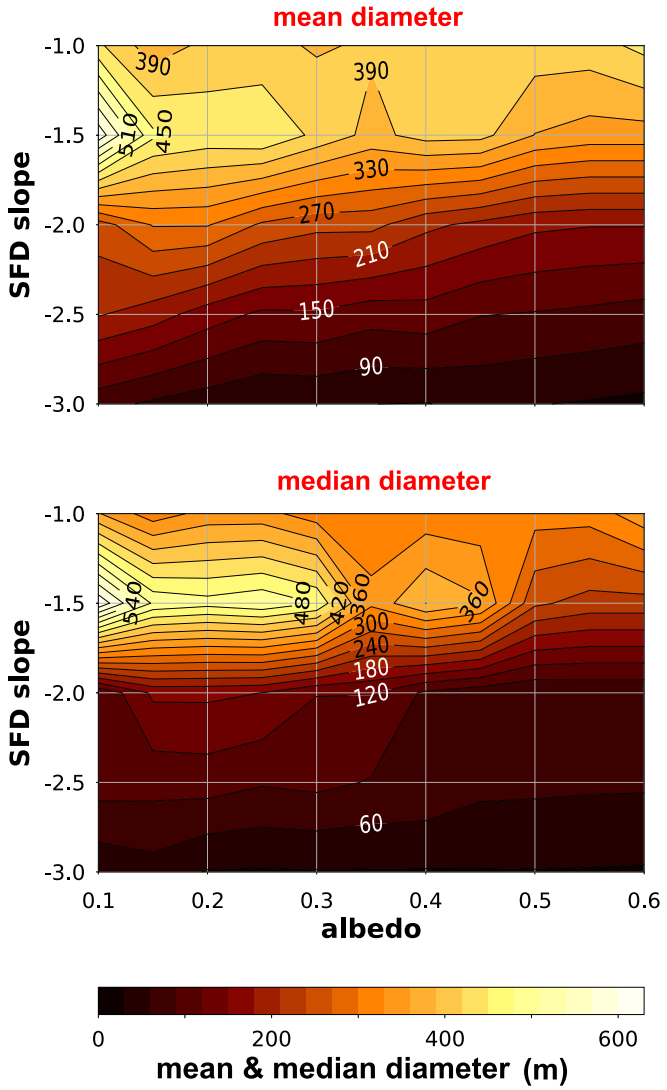

Figure 11. Mean and median diameter of detectable objects.

which they were detected. We also accounted for the trailing loss due to large sky-plane velocities of ISOs.

We found that the overall rate at which the LSST discovers ISOs is sensitive to the SFD slope and albedo of ISOs. The annual rate at which LSST should discover 'Oumuamua-like ISOs ranges from ∼0 to 70 detected objects per year based on the assumptions of the SFD and albedo. The span of this range is considerably broader than some of the previous estimates. For example, Hoover et al. (2022) predicted that the LSST would make one to three ISO detections per year. However, those simulations did not incorporate the SFD of ISOs. Here we have demonstrated that changes in the SFD can substantially increase the number of detectable ISOs and potential targets for rendezvous missions. Additionally, Hoover et al. (2022) assumed that all objects exhibit the same absolute magnitude as 1I/'Oumuamua (22.4). Given that our analysis spans a broad range of SFDs and characteristic albedo values, it has yielded a wider spectrum of potential detection numbers. This bracketed range covers a significant range of solar system populations at small sizes (Grav et al. 2011; Peña et al. 2020), so we can safely assume that the number per year will be within this range.

In this work, we presented results that were intentionally agnostic to the ISO SFD and albedo distribution. This is due to the fact that these parameters are almost entirely unconstrained empirically. Moreover, measurements of the SFDs within and across various small-body populations within the solar system vary and are size limited. If the albedo distribution of ISOs is similar to those measured in asteroids from NASA's Wide-field Infrared Explorer (WISE) mission (in the range of 0.01–0.4; Mainzer et al. 2012), 0–15 ISOs should be detectable per year with LSST.

The apparent rate of motion appears to be the largest issue to overcome for detecting ISOs with the LSST. In Figure 2 it is evident that these objects move very rapidly on the sky. Depending on SFD slope and albedo, the fraction of objects faster than $1^\circ\,\mathrm{day}^{-1}$ ranges from 16% to 85%. Increasing the SFD and decreasing the albedo increases this fraction. In order to link these detections into orbits, a suitable detection algorithm relying on the length and orientation of the trails will be necessary. After accounting for exposure time and expected seeing, it is evident that objects moving faster than $\sim 1^\circ\,\mathrm{day}^{-1}$ will exhibit trailing in LSST images (Fedorets et al. 2020). Therefore, suitable algorithms for trailed detections should be employed to link these detections (Vereš & Chesley 2017). A potential challenge lies in objects with velocities ranging between 0.5 and $1^\circ\,\mathrm{day}^{-1}$. While these objects will not create trails, they exceed the typical suggested velocity threshold of $0^\circ.5\,\mathrm{day}^{-1}$.[6] The fraction of our simulated detections falling within this range varies from 7% to 55%, depending on the kinematics, SFD, and albedos of the population. This strongly suggests the need to increase the velocity threshold in linking algorithms to cover these detections. The use of more efficient algorithms, such as HelioLinC (Holman et al. 2018), has the potential to facilitate this threshold increase and to handle a larger number of tracklets.

An intriguing suggestion from these results is that it may be easier to identify rapidly moving objects outside of the densely populated ecliptic plane. For example, the Antarctic Search for Transiting Exoplanets (ASTEP) project FOV from Antarctica could be ideal for finding ISOs (Hasler et al. 2023). While ISOs will also populate the ecliptic plane, they will be more or less isotropically distributed across the sky for surveys with limiting magnitudes comparable to the LSST. However, detections of ISOs like 1I/'Oumuamua cluster around the ecliptic for less sensitive surveys (Hoover et al. 2022).

It appears that the trailing loss is another major limiting factor on the number of detectable ISOs with the LSST (Figure 1). It is possible that the number density of 'Oumuamua-like objects is higher than currently estimated as a result of a large fraction of ISOs currently undetectable owing to trailing loss and rapid sky motions. To some extent, ISO discovery is similar to NEO discovery. The primary differences are that the spatial distribution of ISOs is isotropic and they exhibit a broader range of sky-plane velocity and acceleration. The development of linking algorithms optimized for rapidly moving objects with trailing loss would be ideal for detecting ISOs.

[6] LSST Moving Object Pipeline System Design: https://docushare.lsst.org/docushare/dsweb/Get/LDM-156/LDM-156.pdf.

Acknowledgments

We thank Ari Heinze, Dave Jewitt, Dong Lai, Matt Payne, and Matt Holman for useful conversations and suggestions. D.Z.S. acknowledges financial support from the National Science Foundation grant No. AST-2107796, NASA grant No. 80NSSC19K0444, and NASA contract NNX17AL71A. D.Z.S. is supported by an NSF Astronomy and Astrophysics Postdoctoral Fellowship under award AST-2202135. This research award is partially funded by a generous gift of Charles Simonyi to the NSF Division of Astronomical Sciences. The award is made in recognition of significant contributions to Rubin Observatory's Legacy Survey of Space and Time. D.M. acknowledges financial support from Ministry of Science, Technological Development and Innovation of the Republic of Serbia, contract No. 451-03-47/2023-01/200104.

ORCID iDs

Dušan Marčeta https://orcid.org/0000-0003-4706-4602
Darryl Z. Seligman https://orcid.org/0000-0002-0726-6480

References

Bagnulo, S., Cellino, A., Kolokolova, L., et al. 2021, NatCo, 12, 1797
Bannister, M. T., Schwamb, M. E., Fraser, W. C., et al. 2017, ApJL, 851, L38
Belton, M. J. S., Hainaut, O. R., Meech, K. J., et al. 2018, ApJL, 856, L21
Bergner, J. B., & Seligman, D. Z. 2023, Natur, 615, 610
Bodewits, D., Noonan, J. W., Feldman, P. D., et al. 2020, NatAs, 4, 867
Bolin, B. T., Bodewits, D., Lisse, C. M., et al. 2020a, ATel, 13613, 1
Bolin, B. T., Lisse, C. M., Kasliwal, M. M., et al. 2020b, AJ, 160, 26
Bolin, B. T., Weaver, H. A., Fernandez, Y. R., et al. 2018, ApJL, 852, L2
Bowell, E., Hapke, B., Domingue, D., et al. 1989, in Asteroids II, ed. R. P. Binzel, T. Gehrels, & M. S. Matthews (Tucson, AZ: Univ. Arizona Press), 524
Brasser, R., Higuchi, A., & Kaib, N. 2010, A&A, 516, A72
Brasser, R., & Morbidelli, A. 2013, Icar, 225, 40
Chambers, K. C., Magnier, E. A., Metcalfe, N., et al. 2016, arXiv:1612.05560
Cook, N. V., Ragozzine, D., Granvik, M., & Stephens, D. C. 2016, ApJ, 825, 51
Cordiner, M. A., Milam, S. N., Biver, N., et al. 2020, NatAs, 4, 861
Cornwall, S., Eggl, S., Juric, M., & Jones, L. 2020, AAS/DPS Meeting, 52, 110.04
de León, J., Licandro, J., Serra-Ricart, M., et al. 2019, RNAAS, 3, 131
Desch, S. J., & Jackson, A. P. 2021, JGRE, 126, e06807
Desch, S. J., & Jackson, A. P. 2022, AsBio, 22, 1400
Do, A., Tucker, M. A., & Tonry, J. 2018, ApJL, 855, L10
Dones, L., Brasser, R., Kaib, N., & Rickman, H. 2015, SSRv, 197, 191
Drahus, M., Guzik, P., Udalski, A., et al. 2020, ATel, 13549, 1
Drahus, M., Guzik, P., Waniak, W., et al. 2018, NatAs, 2, 407
Engelhardt, T., Jedicke, R., Vereš, P., et al. 2017, AJ, 153, 133
Fedorets, G., Granvik, M., Jones, R. L., Jurić, M., & Jedicke, R. 2020, Icar, 338, 113517
Fitzsimmons, A., Meech, K., Matrà, L., & Pfalzner, S. 2023, arXiv:2303.17980
Fitzsimmons, A., Snodgrass, C., Rozitis, B., et al. 2018, NatAs, 2, 133
Flekkøy, E. G., Luu, J., & Toussaint, R. 2019, ApJL, 885, L41
Flekkøy, E. G., & Toussaint, R. 2023, MNRAS Letters, 523, L9
Francis, P. J. 2005, ApJ, 635, 1348
Fraser, W. C., Pravec, P., Fitzsimmons, A., et al. 2018, NatAs, 2, 383
Füglistaler, A., & Pfenniger, D. 2018, A&A, 613, A64
Gaidos, E., Williams, J., & Kraus, A. 2017, RNAAS, 1, 13
Gomes, R. S., Morbidelli, A., & Levison, H. F. 2004, Icar, 170, 492
Grav, T., Jedicke, R., Denneau, L., et al. 2011, PASP, 123, 423
Guzik, P., Drahus, M., Rusek, K., et al. 2020, NatAs, 4, 53
Hahn, J. M., & Malhotra, R. 1999, AJ, 117, 3041
Halder, P., & Sengupta, S. 2023, ApJ, 947, 1
Hallatt, T., & Wiegert, P. 2020, AJ, 159, 147
Hasler, S., Burdanov, A., de Wit, J., et al. 2023, MNRAS, 526, 3601
Higuchi, A., & Kokubo, E. 2015, AJ, 150, 26
Holman, M. J., Payne, M. J., Blankley, P., Janssen, R., & Kuindersma, S. 2018, AJ, 156, 135
Hoover, D. J., Seligman, D. Z., & Payne, M. J. 2022, PSJ, 3, 71
Hopkins, M. J., Lintott, C., Bannister, M. T., Mackereth, J. T., & Forbes, J. C. 2023, AJ, 166, 241
Hsieh, C. H., Laughlin, G., & Arce, H. G. 2021, ApJ, 917, 20
Hui, M. T., Ye, Q. Z., Föhring, D., Hung, D., & Tholen, D. J. 2020, AJ, 160, 92
Ivezić, Ž., Kahn, S. M., & Tyson, J. A. 2019, ApJ, 873, 111
Jackson, A. P., & Desch, S. J. 2021, JGRE, 126, e06706
Jewitt, D., Hui, M. T., Kim, Y., et al. 2020a, ApJL, 888, L23
Jewitt, D., Kim, Y., Mutchler, M., et al. 2020b, ApJL, 896, L39
Jewitt, D., & Luu, J. 1993, Natur, 362, 730
Jewitt, D., & Luu, J. 2019, ApJL, 886, L29
Jewitt, D., Luu, J., Rajagopal, J., et al. 2017, ApJL, 850, L36
Jewitt, D., Mutchler, M., Kim, Y., Weaver, H., & Hui, M. T. 2020c, ATel, 13611, 1
Jewitt, D., & Seligman, D. Z. 2023, ARA&A, 61, 197
Jones, R. L., Chesley, S. R., Connolly, A. J., et al. 2009, EM&P, 105, 101
Jones, R. L., Slater, C. T., Moeyens, J., et al. 2018, Icar, 303, 181
Kaib, N. A., & Quinn, T. 2009, Sci, 325, 1234
Kim, Y., Jewitt, D., Mutchler, M., et al. 2020, ApJL, 895, L34
Knight, M. M., Protopapa, S., Kelley, M. S. P., et al. 2017, ApJL, 851, L31
Laughlin, G., & Batygin, K. 2017, RNAAS, 1, 43
Levine, W. G., Cabot, S. H. C., Seligman, D., & Laughlin, G. 2021, ApJ, 922, 39
Levine, W. G., & Laughlin, G. 2021, ApJ, 912, 3
Luu, J. X., Flekkøy, E. G., & Toussaint, R. 2020, ApJL, 900, L22
Mainzer, A., Grav, T., Bauer, J., et al. 2015, AJ, 149, 172
Mainzer, A., Grav, T., Masiero, J., et al. 2012, ApJL, 760, L12
Mamajek, E. 2017, RNAAS, 1, 21
Marčeta, D. 2023, A&C, 42, 100690
Mashchenko, S. 2019, MNRAS, 489, 3003
Masiero, J. 2017, arXiv:1710.09977
Mazzotta Epifani, E., Dotto, E., Perna, D., et al. 2021, P&SS, 208, 105341
Meech, K. J., Weryk, R., Micheli, M., et al. 2017, Natur, 552, 378
Micheli, M., Farnocchia, D., Meech, K. J., et al. 2018, Natur, 559, 223
Morbidelli, A., Levison, H. F., Tsiganis, K., & Gomes, R. 2005, Natur, 435, 462
Moro-Martín, A. 2019, ApJL, 872, L32
Moro-Martín, A. 2022, arXiv:2205.04277
Moro-Martín, A., Turner, E. L., & Loeb, A. 2009, ApJ, 704, 733
Nesvorný, D. 2018, ARA&A, 56, 137
Oort, J. H. 1950, BAN, 11, 91
Peña, J., Fuentes, C., Förster, F., et al. 2020, AJ, 159, 148
Pravec, P., & Harris, A. W. 2007, Icar, 190, 250
Rice, M., & Laughlin, G. 2019, ApJL, 884, L22
Schwamb, M. E., Jones, R. L., Yoachim, P., et al. 2023, ApJS, 266, 22
Sekanina, Z. 2019a, arXiv:1901.08704
Sekanina, Z. 2019b, arXiv:1905.00935
Seligman, D., & Laughlin, G. 2018, AJ, 155, 217
Seligman, D., & Laughlin, G. 2020, ApJL, 896, L8
Seligman, D. Z., & Moro-Martín, A. 2023, arXiv:2304.00568
Solontoi, M., Ivezić, Ž, & Jones, L 2011, AAS Meeting, 217, 252.11
Trilling, D. E., Robinson, T., Roegge, A., et al. 2017, ApJL, 850, L38
Tsiganis, K., Gomes, R., Morbidelli, A., & Levison, H. F. 2005, Natur, 435, 459
Vereš, P., & Chesley, S. R. 2017, AJ, 154, 12
Williams, G. V., Sato, H., Sarneczky, K., et al. 2017, CBET, 4450, 1
Ye, Q. Z., Zhang, Q., Kelley, M. S. P., & Brown, P. G. 2017, ApJL, 851, L5
Zhang, Q., Ye, Q., & Kolokolova, L. 2020, ATel, 13618, 1